Ultrafast Electrically Tunable Polaritonic Metasurfaces

*Jongwon Lee, Seungyong Jung, Pai-Yen Chen, Feng Lu, Frederic Demmerle, Gerhard Boehm, Markus-Christian Amann, Andrea Alù, and Mikhail A. Belkin**

Electrically tunable mid-infrared metasurfaces with nanosecond response time and broad tuning range are reported. Electrical tuning is achieved by employing strong polaritonic coupling of electromagnetic modes in metallic nanoresonators with voltage-tunable inter-subband transitions in semiconductor heterostructures, tailored for a giant quantum-confined Stark effect. Experimentally, a 220-nm-thick multi-quantum-well semiconductor layer is sandwiched between a ground plane and a metal layer patterned with plasmonic nanoresonators. Approximately 300 nm absorption peak tuning and over 30% absorption change are demonstrated at around 7 μm wavelength at normal incidence by changing the DC bias voltage from 0 to +5 V. Fast reflectivity modulation of the metasurface is shown with a response time less than ~10 ns using bias voltage modulation between +2 V and +4 V. Since the bias affects the optical response at the individual nanoresonator level, this approach may be used to create metasurfaces for ultrafast electrical wavefront tuning and beam steering.

1. Introduction

Plasmonic metasurfaces have recently raised widespread interest due to their ability to control the optical response over a broad spectral range and at deeply sub-wavelength scales by properly tailoring size and shape of metallic nanoinclusions. Frequency selective surfaces[1–3] may be considered the predecessors of metasurfaces, constituted by uniform arrays of inclusions with size of the order of the wavelength capable to tailor the spectral response to a large degree. Introducing plasmonic materials allows drastically squeezing the dimensions of each inclusion and confining light in sub-diffractive volumes, with advantages in terms of spatial resolution and enhanced light control. Recently, the concept of gradient metasurfaces has also emerged, in which metallic nanoinclusions are individually tailored to scatter light with the desired phase and amplitude spatial profile. Gradient metasurfaces provide a much richer control of the wavefront in both local amplitude and phase of the emerging transmitted and reflected beams.[4–7] Such structures enable flat optical components for beam focusing, polarization control and phase correction, to name a few examples.[4–9]

The next challenge and exciting perspective for this technology consists in enabling real-time reconfigurability of the metasurface platform with a fast response time, which may produce flat optical components for rapid wavefront modulation, phase tuning and beam steering.[7] A number of methods to tune the spectral response of plasmonic nanoresonators have been reported in the recent past, based on thermal, mechanical, optical, and electrical control, as summarized in the literature.[10] Electrical tuning techniques are of particular interest, since they open a route to on-chip integration of metasurfaces with electronics, potentially enabling GHz-level switching speeds. The most common electrical tuning mechanisms reported so far are based on phase-change media,[11–13] the use of liquid crystals,[14,15] and carrier concentration control on a semiconductor substrate[16,17] or graphene.[18–23] Approaches based on phase-change media and liquid crystals rely on intrinsically slow physical processes and cannot produce metasurfaces with nanosecond switching time. Carrier-concentration control produces metasurfaces with much faster switching speeds with the best results in terms of tuning range and switching speeds achieved with hybrid metal–graphene structures, demonstrating spectral tuning with switching speeds up to 30 MHz,[23] limited by the RC (circuit resistance × circuit capacitance) time constant of the biasing circuit.

It has recently been suggested and experimentally demonstrated by our team[24,25] as well as by Brener's group in Sandia Labs[26–28] that metasurfaces made of plasmonic nanoresonators polaritonically coupled[29–32] to intersubband transitions in multi-quantum-well (MQW) semiconductor heterostructures engineered for large quantum confined Stark effect[33–35] may display voltage-tunable optical response. Here we demonstrate that these polaritonic metasurfaces may provide one of the fastest electrical switching of optical response demonstrated in metasurfaces to date. Our structures utilize well-established InGaAs/AlInAs MQW semiconductor technology and demonstrate comparable absorption modulation speed compared to hybrid metal–graphene structures while using lower bias

J. Lee, Dr. S. Jung, Dr. P.-Y. Chen, F. Lu,
Prof. A. Alù, Prof. M. A. Belkin
Department of Electrical and Computer Engineering
University of Texas at Austin
Austin, TX 78758, USA
E-mail: mbelkin@ece.utexas.edu
F. Demmerle, G. Boehm, Prof. M.-C. Amann
Walter Schottky Institut
Technische Universität München
Am Coulombwall 4, Garching 85748, Germany

DOI: 10.1002/adom.201400185

modulation voltage.[23] Potential applications of these devices may span across multiple disciplines, including actively controllable fast optical switches, beam steering devices, and ultrafast spatial optical modulators.

In the context of modulation speed, we note that the speed of devices based on carrier-concentration modulation is ultimately limited by the carrier injection/removal time (although the time scales of these processes are in the picosecond range, much smaller than the RC time constants of devices demonstrated to date). In contrast, similar to other modulators based on classical electro-optic effect,[36] the time response of our devices is limited only by the RC time constant of the biasing circuit which may ultimately offer an advantage for achieving very high modulation speeds.

2. Metasurface Design

Quantum engineering of intersubband transitions in *n*-doped MQW heterostructures provides the possibility to produce optical materials with one of the largest known electro-optic coefficients for TM-polarized light, associated with quantum confined Stark effect.[33–35] For optical frequencies ω close to intersubband transition frequency, the dielectric constant for E-field polarization perpendicular to the heterostructure layers can be written as[37]

$$\varepsilon_{\perp}(\omega) \approx \varepsilon_{core}(\omega) + \frac{N_e (e z_{12})^2}{\varepsilon_0 \hbar \left((\omega_{12} - \omega) - i\gamma_{12} \right)} \quad (1)$$

where $\varepsilon_{core}(\omega)$ is the dielectric constant of an undoped semiconductor structure, e is the electron charge, N_e is the average bulk doping density in the MQW structure, and z_{12}, ω_{12}, and γ_{12} are the transition dipole moment, frequency, and linewidth broadening factor, respectively, for a transition between electron states 1 and 2 (see **Figure 1**a,b,c).

MQW structures can be designed to display giant quantum confined Stark effect by tailoring the wavefunctions for states 1 and 2 to be spatially separated (see Figure 1a as an example).[33–35] In this case transition energy ω_{12} can be tuned by bias voltage applied across the structure and this leads to a change in $\varepsilon_{\perp}(\omega)$ (cf. Equation 1). Owing to intrinsic TM-polarization of intersubband transitions between electron states, the value of the dielectric constant for electric field parallel to the MQW layers, $\varepsilon_{//}(\omega)$, stays unchanged. Our structure is designed using a self-consistent Poisson-Schrodinger solver. It is composed of 7 repetitions of a double-quantum-well unit that consist of 4.7 nm and 1.9 nm $In_{0.53}Ga_{0.47}As$ quantum wells, separated by a 1 nm thick $Al_{0.48}In_{0.52}As$ barrier. The units are separated with 20 nm thick $Al_{0.48}In_{0.52}As$ barriers, doped to 3.44×10^{17} cm^{-3} in the central 14 nm section. Compared to ref. [27], much thicker barriers between adjacent coupled-quantum-well units used in our structures resulted in over two orders of magnitude reduction of leakage current density (20 A/cm^2 vs 2600 A/cm^2 in ref. [27]) under operational bias voltage which dramatically reduces Ohmic heating in our structures. Figure 1a-e shows the band-structure as well as calculated real and imaginary parts of $\varepsilon_{\perp}$ for the MQW structure used in this work for bias voltages of 0 and +/–1 V applied across approximately 200-nm-thick MQW layer.

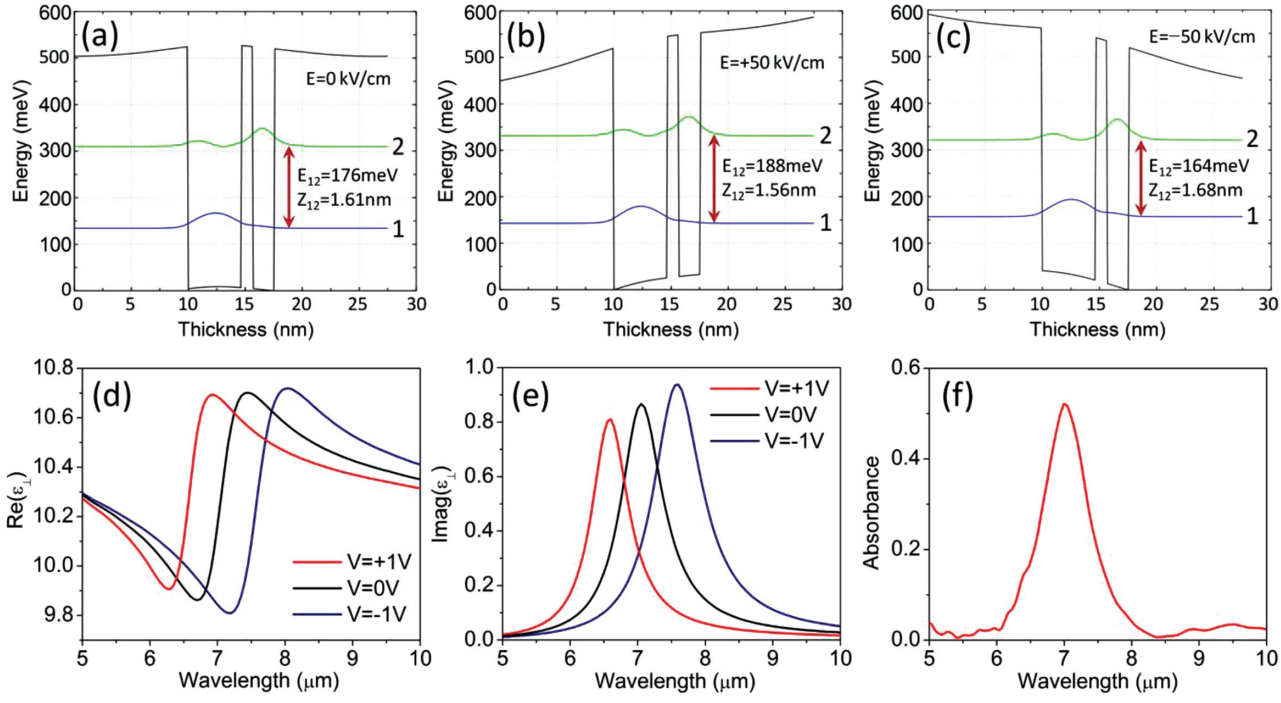

Figure 1. Semiconductor heterostructure design. (a–c) Conduction band diagram of one period of an $In_{0.53}Ga_{0.47}As/Al_{0.48}In_{0.52}As$ coupled MQW structure under zero, +50 kV/cm (+1 V across 200 nm), and –50 kV/cm (–1 V across 200 nm) bias fields. Shown in (a–c) are calculated transition dipole moment z_{12} and transition energy E_{12} between the first two electron subbands. (d,e) Calculated real (d) and imaginary (e) parts of the dielectric constant normal to MQW layers $\varepsilon_{\perp}(\omega)$ under applied bias voltages of 0 and +/–1 V. (f) Measured absorption spectrum of the MQW structure for zero bias at room temperature.

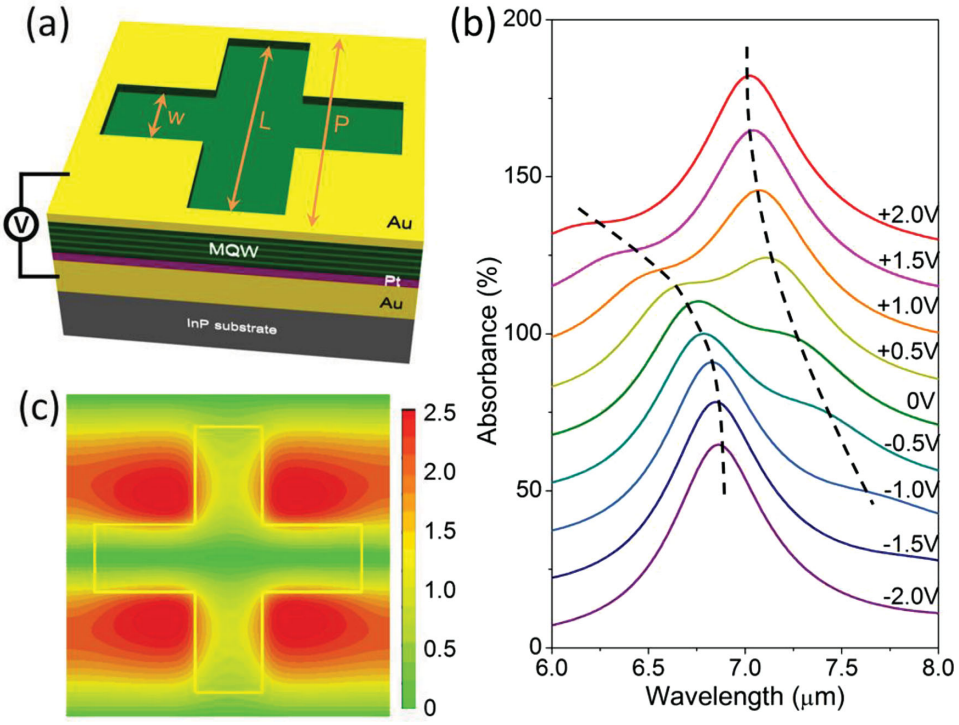

Figure 2. Metasurface design. (a) One unit cell of the periodic metasurface ($w = 0.38$ μm, $L = 1.48$ μm, $P = 1.73$ μm). The semiconductor layer is sandwiched between a top complementary nanocross array and a bottom metal ground plane. Bias voltage is applied across the semiconductor layer with top and bottom metal films acting as electrodes. (b) Simulated metasurface absorption at different bias voltages. Black dash lines trace the positions of the two polaritonic peaks at different DC bias voltages and polaritonic splitting of the absorption peak is clearly visible. For clarity, the absorption curves at different bias voltages are offset from each other vertically by 15%. (c) Simulated distribution of normal electric field component and its enhancement relative to the incident field magnitude in the semiconductor layer 100 nm below the complementary nanocross array. Simulations are performed at $\lambda = 6.75$ μm and zero bias voltage.

The calculations assume doping density $N_e = 1.74 \times 10^{17}$ cm^{-3} and transition linewidth $2\hbar\gamma_{12} \approx 19meV$ obtained from measured intersubband absorption in the MQW structure at zero bias shown in Figure 1f. We note that the absorption peak at $\hbar\omega_{12} \approx 177meV$ in Figure 1f is in excellent agreement with the theoretical calculations shown in Figure 1a.

The MQW layer is then sandwiched between a bottom metal ground plane and a top metal layer patterned with an array of complementary nanocrosses. The unit cell of the metasurface is shown in **Figure 2**a. The bottom ground plane is implemented to ensure that the plasmonic nanoresonators support TM-polarized modes in the MQW layer, and it may, at the same time, be used as bottom electrode for electrical biasing of the MQW structure. The complimentary cross design for the top surface pattern is chosen to produce continuous top metal electrode for biasing.

As follows from Equation 1 and as shown in Figure 1d, the refractive index change is particularly strong for frequencies close to the intersubband transition frequency ω_{12}. Consequently, in order to achieve the maximum tuning range, the complimentary cross nanostructures were designed to have a resonance close to intersubband transition frequency ω_{12} for zero bias. In this case, the electromagnetic modes in metallic nanostructures are polaritonically coupled to the intersubband transition 1–2 in the MQW layer. The polaritonic absorption peak splitting can be seen in the simulated absorption spectra of the metasurface at normal incidence shown in Figure 2b. The vacuum Rabi energy splitting[29,30] is calculated to be $2\hbar\Omega_R = 16.7meV$, in good agreement with simulation results. Figure 2b also shows how the metasurface absorption is expected to change as the transition frequency between electron subbands 1 and 2 is tuned by the bias voltage. Figure 2c shows the distribution of surface normal component of E-field induced in the MQW layer by input light at normal incidence. We note that, due to the symmetry of complimentary nanoscross structures, the same response is achieved for any light polarization at normal incidence. Further details on the simulation procedure are given in the Experimental Section.

3. Results

Experimentally, a 400 μm × 400 μm two-dimensional array of nanoresonators, as shown in Figure 2a, was patterned on top of the MQW layer metal-bonded to a semiconductor substrate. Details of the fabrication process are described in the Experimental Section. The top and bottom metal contact layers were wire bonded to apply a bias voltage. **Figure 3**a–c show a top view of the scanning electron microscope image of the complete wire-bonded device (Figure 3a), details of the top surface pattern (Figure 3b), and a side view of the cleaved facet of the metasurface showing the MQW layer above the metal

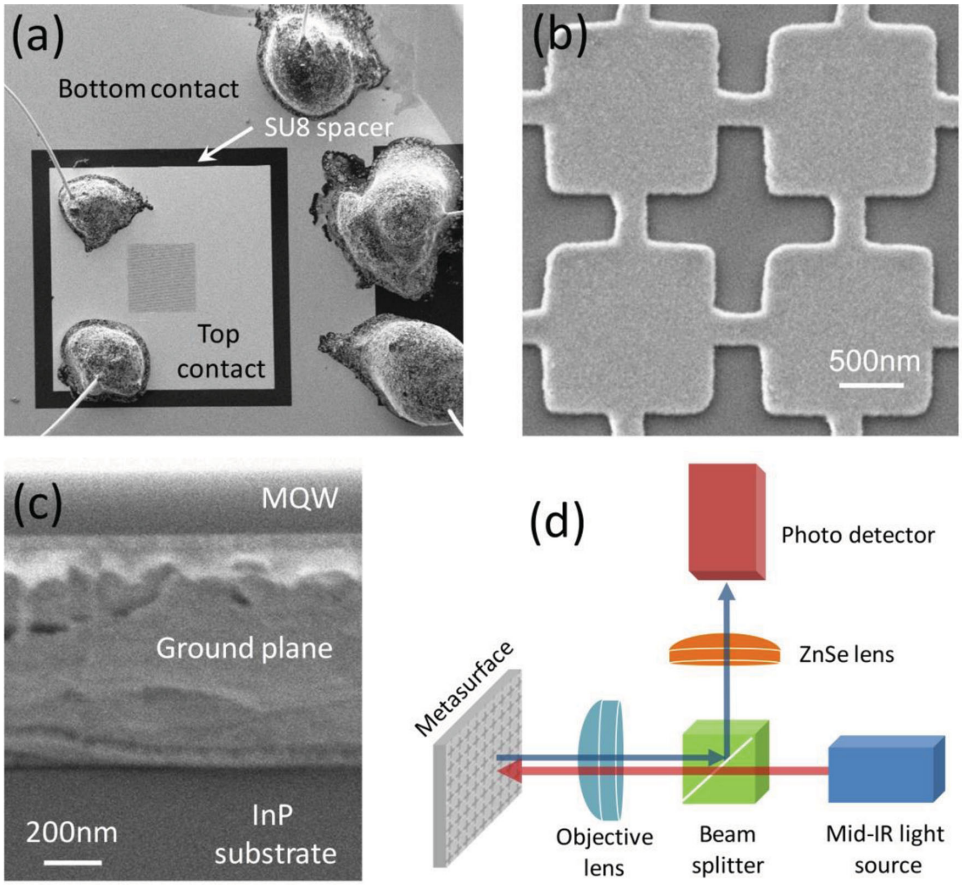

Figure 3. Fabricated metasurface and experimental measurement setup. (a–c) Scanning electron microscope images of the wire-bonded device (a), the complementary crosses (b), and a side view of the cleaved facet with the MQW layer metal-bonded to InP substrate (c). (d) Optical setup used for characterization. Mid-IR light source can be either a broadband thermal output from a Fourier-transform infrared spectrometer or a broadly tunable quantum cascade laser.

ground plane bonded to a substrate (Figure 3c). A schematic of the optical setup for our measurements is illustrated in Figure 3d.

For initial characterization, we measured absorption spectra of the metasurface for different applied DC bias voltages from −5 V to +5 V with a 1 V step. The data is shown in **Figure 4**a. The intersubband transition frequency ω_{21} increases with the DC bias, consistent with Figure 1, and this is reflected in the variation of the absorption spectrum. The measured peak absorption shifts by over 0.3 μm from 6.78 μm to 7.09 μm with a change in bias voltage of only 2 V between +1 V and +3 V. Current–voltage measurements of the metasurface in Figure 4b reveal very low current density below 20 A/cm^2 for up to 5 V bias voltage. Simulation of a temperature increase in our structures due to electrical power dissipation shows only 0.04 °C temperature increase under +5 V DC biasing, which shows that our structures require no cooling system for operation.

The experimentally observed spectra in Figure 4a are in good agreement with our simulations in Figure 2b, although higher bias voltages were required to experimentally realize optical tuning. This is most likely the effect of contact resistance at the semiconductor-metal interfaces in the top and bottom electrodes. We note that, due to small thickness of the semiconductor heterostructures of our metasurfaces, we did not use heavily doped 'contact layers' and our contacts are non-alloyed.

Figure 4c shows the variation of metasurface absorbance for different DC bias voltages, defined as $(A_{V_{DC}} - A_{V_{DC}=0V})/A_{V_{DC}=0V}$, where $A_{V_{DC}=0V}$ and $A_{V_{DC}}$ are the metasurface absorbance in percent for zero bias, and applied voltage V, respectively. Strong metasurface absorbance (or reflectivity) modulation is achieved around 6.72 μm and 7.12 μm wavelengths. In particular, over 30% of absorbance change is achieved around 7.12 μm wavelength by changing bias voltage from 0 V to +5 V. Since the tuning is achieved by electro-optic effects due to Stark shift of the intersubband transition energy and it requires no carrier transport across MQW layer, the frequency response of the device is only determined the RC time constant of the biasing circuit.

Ultrafast reflectivity switching was verified by observing intensity variation of the reflected quantum casade laser light at $\lambda = 6.75$ μm, close to the strong intensity modulation region measured in Figure 4c. The bias voltage on the structure was modulated between +2 V and +4 V as confirmed by the oscilloscope traces shown in Figure 4d. To achieve such voltage modulation, we sent short pulses with +2 V amplitude through bias tee with +2 V DC bias. The RC time constant of our structure for such modulation is calculated to be approximately 8 ns using the average structure resistance of approximately 60 Ω in

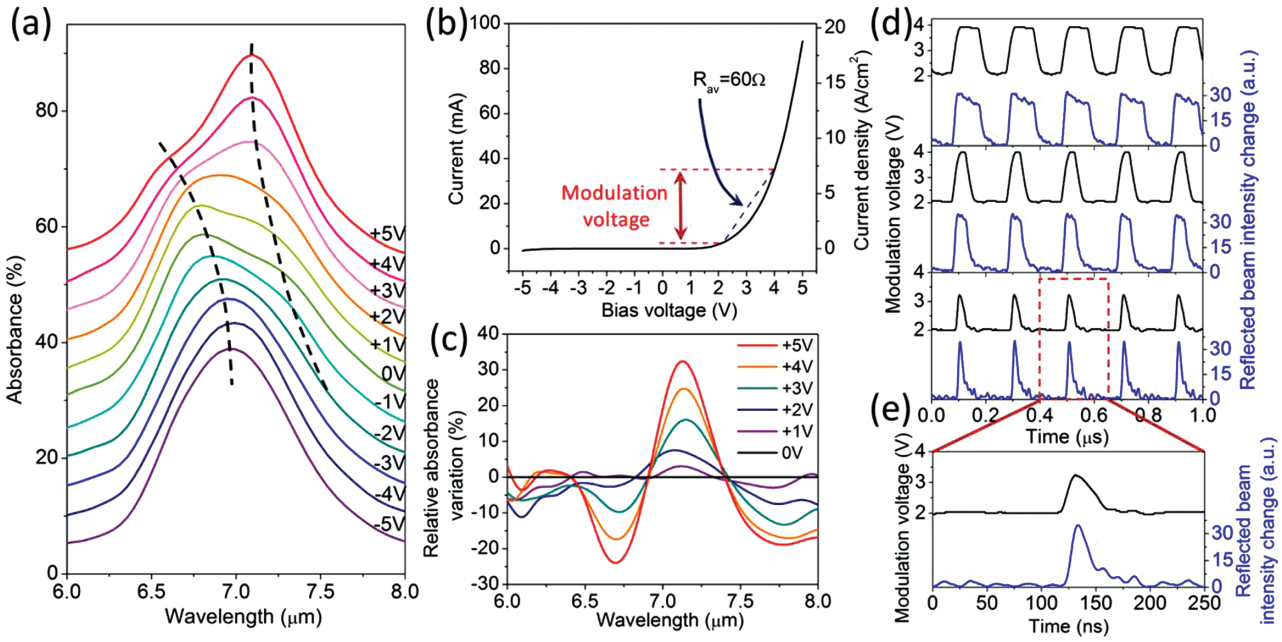

Figure 4. Experimental results. (a) Experimental absorption spectra of the metasurface for different DC bias voltages. For clarity, the absorption curves at different bias voltages are offset from each other vertically by 5%. Black dash lines trace the positions of the two polaritonic peaks at different DC bias voltages. (b) Current–voltage characteristic of the metasurface. (c) Absorption amplitude modulation for positive DC bias voltages deduced from (a). (d) High speed modulation measurements. Oscilloscope traces of the modulation voltage on the metasurface and the corresponding light intensity modulation of the reflected beam are shown. All intensity modulation traces use the same units and background intensity were subtracted for clarity. We applied voltages pulses with different pulse widths: 100 ns (top panel), 50 ns (middle panel), and 10 ns (bottom panel) at 5 MHz repetition frequency. (e) Zoom-in of the data for metasurface modulation with 10 ns pulses.

+2 ~ 4 V range obtained from the current–voltage characteristics shown in Figure 4b and the structure capacitance of 140 pF calculated using the structure dimensions in the Experimental Section. We note that the RC time constant of our metasurface may be significantly improved by reducing the nanoresonator array and contact area sizes. A thermoelectrically cooled mercury cadmium telluride detector with response time of 1 ns was used to detect the intensity modulation of the reflected light. Figure 4d shows oscilloscope traces of the reflected light intensity and corresponding traces showing voltage modulation on the metasurface. Modulation voltage pulses of 100 ns, 50 ns, and 10 ns were sent to the metasurface at 5 MHz repetition frequency and the data shows that reflected beam intensity follows the shape of the voltage pulses with high accuracy. Modulation depth of the reflected light intensity stays approximately constant for all pulse durations as seen in Figure 4d. We note that the voltage pulse width of 10 ns is the minimum pulse width that was available from the pulser in our laboratory, and the measured signals indicate that much faster modulation speeds may be achieved with these polaritonic metasurfaces, since, fundamentally, the response time is only limited by the RC time constant of the associated circuitry.

4. Conclusion

Tunable polaritonic metasurfaces presented in this work represent a new class of ultra-fast reconfigurable metamaterials that achieve the desired optical properties by polaritonic coupling of quantum-engineered transitions between electronic states with electromagnetically engineered modes of metallic nanoresonators. Our design approach allows producing metasurfaces with new functionalities, such as rapidly tunable optical response plasmonic nanoresonators reported here, as well as large optical nonlinearities[39] and signal amplification in electrically pumped structures. Compared to tunable metasurface based on hybrid metal–graphene structures, which have attracted significant attention recently,[18–23] the metasurfaces presented here offer the significant advantages of lower modulation voltages, robust and well-established fabrication technology, and potentially larger modulation speeds. Since tuning in our structures is achieved by an electro-optic effect that requires no electron transport in the MQW layers, the modulation speed may be pushed well within the GHz range and above. The experimental results reported here represent a proof-of-concept experimental demonstration, and we expect further improvements in speed and intensity modulation depth in future structures based on smaller-sized elements with reduced RC time constant and optimized nanoresonators designs. The metasurface geometry presented here is well-suited for integration into various voltage-reconfigurable flat optical elements for, e.g., real-time beam steering and polarization control using polarization-sensitive plasmonic nanoresonators.

5. Experimental Section

Numerical Calculations: Commercial Maxwell's equations solver (CST studio) based on the finite-integration method in frequency domain was used to compute the reflectance and E-field distribution in the MQW

layer. Periodic boundary conditions were placed around the unit cell and open boundary conditions were placed in the perpendicular direction of the top device surface. Because of the ground plane, the transmittance of the metasurface was zero and the absorbance A was calculated as $A = 1 - R$, where R is the power reflectance of the metasurface.

Device Fabrication: MQW structures were grown by the molecular beam epitaxy on a semi-insulating InP substrate. The growth started with 300-nm-thick etch-stop layer of $In_{0.53}Ga_{0.47}As$, followed by a 100-nm-thick etch-stop layer of InP, followed the MQW structure. A 10-nm-thick layer of titanium, a 50-nm-thick layer of platinum, and a 500-nm-thick layer of gold were subsequently evaporated on top of the MQW layer. The wafer was then thermo-compressively bonded epi-side down to a semi-insulating InP wafer coated with same metal layers. The InP substrate on the MQW wafer was then removed via selective etching, followed by the removal of the etch-stop layers via selective etching. A 400 μm by 400 μm array of complementary crosses was produced on the MQW layer with e-beam lithography, evaporation of a 5-nm-thick layer of titanium and 40-nm-thick layer of gold, and lift-off. A 700 μm by 700 μm of square mesa structure was then etched in the MQW layer all the way to the bottom metal contact layer with the patterned complimentary cross array in the center of the mesa. A 1.5 mm by 1.5 mm square patch made of 500-nm thick layer of SU-8 photoresist was then deposited on top of the mesa and surrounding area with a 400 μm by 400 μm of square opening on top of the nanocross array. Finally, a 1.4 mm by 1.4 mm top metal contact layer with a window across the nanocross pattern was fabricated on top of the SU-8 patch. The contact layer is made of a 10-nm-thick layer of titanium and 150-nm-thick layer of gold and it contacts with the borders of the nanocross array. Finally the device was mounted on a copper block and wire-bonded to produce the structure shown in Figure 3a.

The total device capacitance of the structure is calculated by summing the capacitance of a 400×400 μm^2 section of nanocrosses on 220 nm MQW layer, 700×700 μm^2 of mesa section with 500-nm-thick layer of SU-8 on top of the 220 nm MQW layer, less 400×400 μm^2 center section, and 1.4×1.4 mm^2 500-nm-thick layer of SU-8 on top of ground plane, less the 700×700 μm^2 mesa structure. The dielectric constant of the MQW layer was taken to be $\varepsilon_{MQW} \approx 10$ from ref. [38] and that of SU-8 was taken to be $\varepsilon_{SU-8} \approx 2.5$ from the manufacturer specifications sheet (Microchem Corp.).

Experimental Measurements: A schematic of the experimental setup is shown in Figure 3b. A Fourier-transform infrared spectrometer (FTIR) was used for the spectral measurement of the finished device. Broadband mid-infrared light from the FTIR thermal source passed through a chopper and a non-polarizing achromatic 50% beam splitter, and was focused on a sample at normal incidence through a numerical aperture 0.5 lens. The reflected signal was collected by the same objective lens and was directed by the beam splitter towards a liquid nitrogen cooled mercury cadmium telluride (MCT) photo-detector (Kolmar Technologies, Inc) through another lens. The reflection spectrum from a metasurface was normalized using reflected signal from a gold mirror as a reference.

For our high-frequency modulation measurements, a continuous-wave broadly tunable quantum cascade laser (Daylight Solutions, Inc.) was used instead of an FTIR thermal source and a fast mid-IR photovoltaic mercury cadmium telluride (MCT) detector (Vigo System S.A., time constant < 1 ns) was used instead of slow cryogenically cooled MCT detector in the optical setup described earlier and shown in Figure 3b. Voltage pulses across the metasurface and the modulated signal from the MCT detector were monitored simultaneously on the multi-channel oscilloscope.

Acknowledgements

This work has been supported by the AFOSR YIP award No. FA9550–10–1–0076 (to M.A.B.), AFOSR YIP award No. FA9550–11–1–0009 (to A.A.), the NSF EAGER grant No. 1348049 (to M.A.B. and A.A.), and the ONR MURI grant No. N00014–10–1–0942 (to A.A.). Walter Schottky Institute group acknowledges support from the excellence cluster 'Nano Initiative Munich (NIM)'. Sample fabrication was carried out in the Microelectronics Research Center at the University of Texas at Austin, which is a member of the National Nanotechnology Infrastructure Network.

Received: April 23, 2014
Revised: June 24, 2014
Published online: July 30, 2014

[1] X. L. Liu, T. Starr, A. F. Starr, W. J. Padilla, *Phys. Rev. Lett.* **2010**, *104*, 207403.
[2] B. A. Munk, *Frequency Selective Surfaces: Theory and Design*, Wiley, New York, **2000**.
[3] T. K. Wu, *Frequency Selective Surface and Grid Array*, Wiley, New York **1995**.
[4] N. F. Yu, P. Genevet, M. A. Kats, F. Aieta, J. P. Tetienne, F. Capasso, Z. Gaburro, *Science* **2011**, *334*, 333.
[5] X. J. Ni, N. K. Emani, A. V. Kildishev, A. Boltasseva, V. M. Shalaev, *Science* **2012**, *335*, 427.
[6] A. V. Kildishev, A. Boltasseva, V. M. Shalaev, *Science* **2013**, *339*, 12320091.
[7] N. F. Yu, F. Capasso, *Nat. Mater.* **2014**, *13*, 139.
[8] C. Pfeiffer, A. Grbic, *Phys. Rev. Lett.* **2013**, *110*, 197401.
[9] F. Monticone, N. M. Estakhri, A. Alu, *Phys. Rev. Lett.* **2013**, *110*, 203903.
[10] N. I. Zheludev, Y. S. Kivshar, *Nat. Mater.* **2012**, *11*, 917.
[11] T. Driscoll, H. T. Kim, B. G. Chae, B. J. Kim, Y. W. Lee, N. M. Jokerst, S. Palit, D. R. Smith, M. Di Ventra, D. N. Basov, *Science* **2009**, *325*, 1518.
[12] H. T. Chen, H. Yang, R. Singh, J. F. O'Hara, A. K. Azad, S. A. Trugman, Q. X. Jia, A. J. Taylor, *Phys. Rev. Lett.* **2010**, *105*, 247402.
[13] Z. L. Samson, K. F. MacDonald, F. De Angelis, B. Gholipour, K. Knight, C. C. Huang, E. Di Fabrizio, D. W. Hewak, N. I. Zheludev, *Appl. Phys. Lett.* **2010**, *96*, 143105.
[14] Q. Zhao, L. Kang, B. Du, B. Li, J. Zhou, H. Tang, X. Liang, B. Z. Zhang, *Appl. Phys. Lett.* **2007**, *90*, 011112.
[15] O. Buchnev, J. Y. Ou, M. Kaczmarek, N. I. Zheludev, V. A. Fedotov, *Opt. Express* **2013**, *21*, 1633.
[16] H. T. Chen, W. J. Padilla, J. M. O. Zide, A. C. Gossard, A. J. Taylor, R. D. Averitt, *Nature* **2006**, *444*, 597.
[17] W. L. Chan, H. T. Chen, A. J. Taylor, I. Brener, M. J. Cich, D. M. Mittleman, *Appl. Phys. Lett.* **2009**, *94*, 213511.
[18] L. Ju, B. S. Geng, J. Horng, C. Girit, M. Martin, Z. Hao, H. A. Bechtel, X. G. Liang, A. Zettl, Y. R. Shen, F. Wang, *Nat. Nanotechnol.* **2011**, *6*, 630.
[19] S. H. Lee, M. Choi, T. T. Kim, S. Lee, M. Liu, X. Yin, H. K. Choi, S. S. Lee, C. G. Choi, S. Y. Choi, X. Zhang, B. Min, *Nat. Mater.* **2012**, *11*, 936.
[20] Z. Y. Fang, S. Thongrattanasiri, A. Schlather, Z. Liu, L. L. Ma, Y. M. Wang, P. M. Ajayan, P. Nordlander, N. J. Halas, F. J. G. de Abajo, *ACS Nano* **2013**, *7*, 2388.
[21] Y. Yao, M. A. Kats, P. Genevet, N. F. Yu, Y. Song, J. Kong, F. Capasso, *Nano Lett.* **2013**, *13*, 1257.
[22] N. K. Emani, T. F. Chung, A. V. Kildishev, V. M. Shalaev, Y. P. Chen, A. Boltasseva, *Nano Lett.* **2014**, *14*, 78.
[23] Y. Yao, M. A. Kats, R. Shankar, Y. Song, J. Kong, M. Loncar, F. Capasso, *Nano Lett.* **2014**, *14*, 214.
[24] M. A. Belkin, Proc. of the Tri-Service Metamaterials Program Review, Virginia, USA, May 22–25, **2012**.
[25] J. Lee, P.-Y. Chen, C. Argyropoulos, A. Alu, M. A. Belkin, Proc. of the 7th International Congress on Advanced Electromagnetic Materials in Microwaves and Optics – Metamaterials in Bordeaux, France, September 16–21, **2013**.

[26] A. Gabbay, I. Brener, *Opt. Express* **2012**, *20*, 6584.
[27] A. Benz, I. Montano, J. F. Klem, I. Brener, *Appl. Phys. Lett.* **2013**, *103*, 263116.
[28] I. Brener, Proc. of the 7th International Congress on Advanced Electromagnetic Materials in Microwaves and Optics – Metamaterials 2013 in Bordeaux, France, September 16–21, **2013**.
[29] D. Dini, R. Kohler, A. Tredicucci, G. Biasiol, L. Sorba, *Phys. Rev. Lett.* **2003**, *90*, 116401.
[30] Y. Todorov, A. M. Andrews, I. Sagnes, R. Colombelli, P. Klang, G. Strasser, C. Sirtori, *Phys. Rev. Lett.* **2009**, *102*, 186402.
[31] Y. Todorov, A. M. Andrews, R. Colombelli, S. De Liberato, C. Ciuti, P. Klang, G. Strasser, C. Sirtori, *Phys. Rev. Lett.* **2010**, *105*, 196402.
[32] P. Jouy, A. Vasanelli, Y. Todorov, A. Delteil, G. Biasiol, L. Sorba, C. Sirtori, *Appl. Phys. Lett.* **2011**, *98*, 231114.
[33] A. Harwit, J. S. Harris, *Appl. Phys. Lett.* **1987**, *50*, 685.
[34] D. A. Holm, H. F. Taylor, *IEEE J. Quantum Electron.* **1989**, *25*, 2266.
[35] Y. J. Mii, R. P. G. Karunasiri, K. L. Wang, M. Chen, P. F. Yuh, *Appl. Phys. Lett.* **1990**, *56*, 1986.
[36] A. Melikyan, L. Alloatti, A. Muslija, D. Hillerkuss, P. C. Schindler, J. Li, R. Palmer, D. Korn, S. Muehlbrandt, D. Van Thourhout, B. Chen, R. Dinu, M. Sommer, C. Koos, M. Kohl, W. Freude, J. Leuthold, *Nat. Photonics* **2014**, *8*, 229.
[37] H. C. Liu, F. Capasso, *Intersubband Transitions in Quantum Wells: Physics and Device Applications II*, Academic Press, San Diego, **2000**.
[38] S. Adachi, *Handbook on Physical Properties of Semiconductors: III-V Compound Semiconductors*, Vol. *2*, Springer, Boston, **2004**.
[39] J. Lee, M. Tymchenko, C. Argyropoulos, P.-Y. Chen, F. Lu, F. Demmerle, G. Boehm, M.-C. Amann, A. Alu, M. A. Belkin, *Nature* **2014**, *511*, 65–69.